CHEMISTRY

Two orders of magnitude enhancement in oxygen evolution reactivity on amorphous $Ba_{0.5}Sr_{0.5}Co_{0.8}Fe_{0.2}O_{3-\delta}$ nanofilms with tunable oxidation state

Gao Chen,[1] Wei Zhou,[1]* Daqin Guan,[1] Jaka Sunarso,[2] Yanping Zhu,[1] Xuefeng Hu,[1] Wei Zhang,[1] Zongping Shao[3,4]*

Perovskite oxides exhibit potential for use as electrocatalysts in the oxygen evolution reaction (OER). However, their low specific surface area is the main obstacle to realizing a high mass-specific activity that is required to be competitive against the state-of-the-art precious metal–based catalysts. We report the enhanced performance of $Ba_{0.5}Sr_{0.5}Co_{0.8}Fe_{0.2}O_{3-\delta}$ (BSCF) for the OER with intrinsic activity that is significantly higher than that of the benchmark IrO_2, and this result was achieved via fabrication of an amorphous BSCF nanofilm on a surface-oxidized nickel substrate by magnetron sputtering. The surface nickel oxide layer of the Ni substrate and the thickness of the BSCF film were further used to tune the intrinsic OER activity and stability of the BSCF catalyst by optimizing the electronic configuration of the transition metal cations in BSCF via the interaction between the nanofilm and the surface nickel oxide, which enables up to 315-fold enhanced mass-specific activity compared to the crystalline BSCF bulk phase. Moreover, the amorphous BSCF–Ni foam anode coupled with the Pt–Ni foam cathode demonstrated an attractive small overpotential of 0.34 V at 10 mA cm^{-2} for water electrolysis, with a BSCF loading as low as 154.8 μg cm^{-2}.

INTRODUCTION

Efficient energy conversion and fuel production via the electrochemical systems offer more sustainable energy generation pathways for the near future than the fossil fuel combustion–based systems (*1*–*3*). The oxygen evolution reaction (OER) is a key half-reaction in hydrogen-oxygen electrolyzers, rechargeable metal-air batteries, and regenerative fuel cells. However, the OER is kinetically sluggish and requires a catalyst presence (*4*–*6*). In particular, the OER in an alkaline solution can be represented as $4OH^- \rightarrow O_2 + 2H_2O + 4e^-$, which typically occurs at an overpotential larger than 0.5 V [defined as the difference between the required potential and the thermodynamic potential for the water-splitting reaction of 1.23 V versus the reversible hydrogen electrode (RHE)] (*6*–*8*). Previous studies have established that the OER activity is closely related to the binding strength of the OER intermediates (for example, OH^-) on the catalyst surfaces (*9*, *10*).

In general, perovskite oxides with a general formula of ABO_3, where *A* is a rare earth or an alkaline metal and *B* is a transition metal, exhibit high electrocatalytic activities. Among these oxides, $Ba_{0.5}Sr_{0.5}Co_{0.8}Fe_{0.2}O_{3-\delta}$ (BSCF) is one of the most attractive compounds, and it was initially used as a high-performance oxygen ionic transport membrane and cathode in solid oxide fuel cells (*11*, *12*). Recently, Suntivich *et al.* (*13*) reported that BSCF exhibits a very high OER activity at room temperature in an alkaline solution due to its optimal e_g orbital filling. In addition, the OER activity of BSCF increased with electrochemical cycling due to the amorphization of the surface layers (*8*). In another study, an amorphous quaternary Ba-Sr-Co-Fe oxide, which was prepared using a photochemical deposition route, exhibited a higher OER activity relative to its crystalline counterpart, which indicates that amorphous BSCF is a promising OER electrocatalyst (*14*). Nevertheless, perovskite oxides are typically present as large bulk particles due to their high crystallization temperature. This property also applies to amorphous BSCF, which tends to form thick, bulk films (*14*). Because of the surface origin of the electrochemical reactions, this bulk structure, which contains a large portion of inactive atoms in its bulk, typically exhibits a low mass activity. To minimize this inactive portion, supported two-dimensional (2D) nanofilm catalysts have been fabricated (*15*, *16*). For example, Shao-Horn group successfully deposited a BSCF-decorated $La_{0.8}Sr_{0.2}MnO_{3-\delta}$ (LSM) thin-film electrocatalyst on top of a Nb-doped $SrTiO_3$ substrate, and the mass-specific activity and stability of BSCF on this film were significantly improved relative to its bulk version without influencing the intrinsic activity of BSCF (*15*).

The intrinsic activity of transition metal oxides is closely associated with the electron configuration of the transition metals, which determines the binding strength of the reaction intermediates to the oxide surface (*17*–*20*). Currently, no efficient approach is available to tune the oxidation state of the transition metal in the 2D thin film to achieve an optimized state for catalysis. Here, we use magnetron sputtering deposition to fabricate amorphous BSCF nanofilms that contain transition metal cations with a tunable oxidation state, and these films exhibit ultrahigh mass activity that is 315 times that exhibited by the bulk BSCF particle. Furthermore, we demonstrate that a specific reduction-oxidation interaction exists between the nickel oxide on the Ni substrate and the amorphous BSCF layer, and this interaction plays a critical role in tuning the electronic configuration of the cobalt and iron cations. The electronic configuration of the transition metal cations can be optimized by adjusting the film thickness, allowing control of the intrinsic OER activity and stability. These results also demonstrate that highly stable and efficient water-splitting performance can be achieved by operating our 20-nm BSCF–Ni foam (for OER) in tandem with 10-nm Pt–Ni foam [for hydrogen evolution reaction (HER)], and an overpotential of 0.34 V at 10 mA cm^{-2} for the water electrolysis was realized with a BSCF loading as low as 154.8 μg cm^{-2}. This study highlights a new strategy

[1]Jiangsu National Synergetic Innovation Center for Advanced Materials, State Key Laboratory of Materials-Oriented Chemical Engineering, College of Chemical Engineering, Nanjing Tech University, No. 5 Xin Mofan Road, Nanjing 210009, P. R. China. [2]Faculty of Engineering, Computing and Science, Swinburne University of Technology, Jalan Simpang Tiga, 93350 Kuching, Sarawak, Malaysia. [3]Jiangsu National Synergetic Innovation Center for Advanced Materials, State Key Laboratory of Materials-Oriented Chemical Engineering, College of Energy, Nanjing Tech University, Nanjing 210009, P. R. China. [4]Department of Chemical Engineering, Curtin University, Perth, Western Australia 6845, Australia.
*Corresponding author. Email: zhouwei1982@njtech.edu.cn (W. Zhou); shaozp@njtech.edu.cn (Z.S.)

for efficiently controlling the electronic configuration of electrocatalysts to achieve highly robust and efficient OER performance with very low catalyst loading.

RESULTS

Fabrication and characterization of the BSCF nanofilms

We deposited the amorphous BSCF nanofilm onto the substrates using radio frequency (rf) magnetron sputtering. The powder x-ray diffraction (XRD) pattern confirmed that the phase of the disk target corresponds to the crystalline BSCF perovskite (fig. S1). The amorphous nature of the deposited film became apparent upon inspection of the powder XRD pattern for the 200-nm-thick film on Ni foil because this pattern contains only the characteristic peaks of Ni substrate with no visible peaks corresponding to the characteristics of crystalline BSCF (Fig. 1A). The amorphous nature of the thin film was also confirmed on the basis of their Raman spectra (Fig. 1B). The Raman spectra of the bulk BSCF particles contain a broad peak at approximately 675 cm^{-1}, which was assigned to the internal motion of the oxygen within the CoO_6 and FeO_6 octahedra (*21*). For the 10- to 20-nm-thick films, the vibrational modes were substantially broadened, which is consistent with previous amorphous BSCF results (*8*). In addition, the x-ray photoelectron spectra (XPS) revealed the presence of Ni 2p peaks from the Ni substrate and 1-nm BSCF-Ni sample, which disappear when the amorphous nanofilm thickness was increased to 5 nm (Fig. 1C). This result indicated the complete coverage of Ni by the amorphous BSCF nanofilm in the 5-nm BSCF-Ni case.

The surface morphology of the BSCF film was simultaneously probed using atomic force microscopy (AFM) and scanning electron microscopy (SEM), as shown in figs. S2 and S3A, respectively. The uniform coverage of the substrate by the dense thin film with low variation in the surface roughness indicates that the surface area contribution to the electrocatalytic activity of these films is almost negligible. For an objective comparison, the intrinsic activity of thin films was normalized to the specific area surface (fig. S2). Despite their amorphous nature, the elemental ratio of Ba/Sr/Co/Fe in these films closely corresponds to the stoichiometric ratio for BSCF (0.5:0.5:0.8:0.2), as revealed by the energy-dispersive x-ray spectroscopic result (fig. S3B). The real film thicknesses of the amorphous BSCF nanofilms were obtained from the SEM images over the film substrate cross section (fig. S4). The mass loading of the BSCF catalyst varies from 1.4 to 38.7 μg cm^{-2} for the 1- to 20-nm BSCF–Ni foil heterostructures (table S1).

OER activity measurements

The amorphous BSCF nanofilm deposited on Ni foil was used as the working electrode in the OER test. The measured OER current was

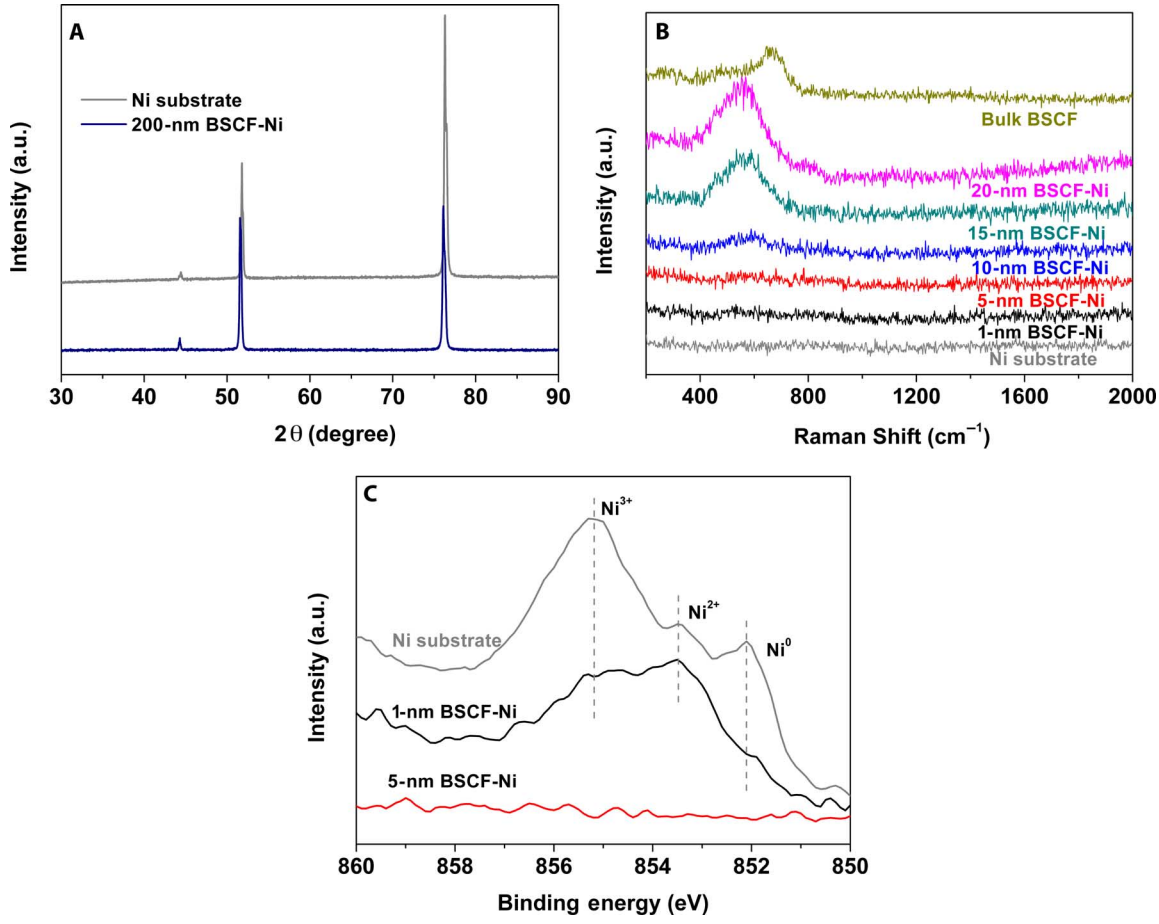

Fig. 1. Characterization of amorphous BSCF nanofilms on Ni foil substrates. (**A**) Powder XRD patterns for the 200-nm BSCF–Ni foil and the Ni foil substrate. (**B**) Raman spectra for the 1-, 5-, 10-, 15-, and 20-nm BSCF on Ni foil as well as the Ni foil substrate and BSCF particle for reference. (**C**) Ni 2p XPS for the Ni foil as well as 1- and 5-nm BSCF–Ni foil heterostructures.

corrected by averaging the currents obtained from the positive (forward) and negative (backward) scans. The ohmic contribution was also subtracted from the measured potential so that the OER plots exhibited the capacity-corrected current as a function of the ohmic-corrected potential scale. The OER polarization curves for different amorphous BSCF nanofilms in an O_2-saturated 0.1 M KOH solution at room temperature are shown in Fig. 2. Figure 2A shows the mass-normalized OER activities at different potentials as a function of the BSCF nanofilm thickness. The Ni foil exhibited negligible OER activity up to 1.9 V versus RHE. The as-deposited BSCF nanofilms exhibited ultrahigh OER mass activities. The lowest OER mass activity of 271 mA mg^{-1} at an overpotential of 0.5 V was obtained for the 20-nm-thick BSCF film, but this value is still 9.5 times larger than that of the bulk BSCF particle (table S1). The obtained mass activity increased quickly as the film thickness decreased and reached a maximum of 9006 mA mg^{-1} at an overpotential of 0.5 V, which is 315 times higher than that of the bulk BSCF particle and is much higher than most of the other available OER catalysts in alkaline solutions (table S1). This maximum mass activity obtained here is comparable to that of the state-of-the-art IrO_2 nanoparticles (*22*) and is much better than that of the commercial bulk IrO_2 (table S1). The characterization details of commercial bulk IrO_2 are displayed in fig. S5. The extraordinary OER mass activities demonstrated by these non–precious metal–based nanofilm catalysts highlight their excellent potential for water splitting, especially via enabling ultralow catalyst loading.

A comparison of the geometric electrode area (corrected by AFM)–normalized OER activity provides additional insight [that is, comparison of their intrinsic catalytic activities (mA cm^{-2}_{film})]. As shown in Fig. 2B, the OER signal contribution from the Ni foil substrate is negligible below 1.65 V versus RHE. The OER activities were substantially enhanced after the amorphous BSCF nanofilms were deposited on the Ni foil substrate. The most negative onset potential was obtained for the 10-nm-thick BSCF film. Furthermore, it is important to compare the relative values of the overpotential (η) required to achieve a current density of 10 mA cm^{-2}_{film}, which is a metric relevant to solar fuel synthesis (*23*, *24*). The overpotentials required to obtain this particular current density decreased in the following order: Ni foil substrate (0.62 V), 20-nm-thick film (0.5 V), 1- and 5-nm-thick films (0.49 V), 15-nm-thick film (0.48 V), and 10-nm-thick film (0.46 V). IrO_2, which is the benchmark OER catalyst, required an overpotential of 0.5 V to reach a current density of 10 mA cm^{-2}_{disc}. For intrinsic activity, a larger overpotential was required to reach a current density of 10 mA cm^{-2}_{oxide} for IrO_2. At this overpotential (η = 0.5 V), the current density of the 10-nm-thick BSCF film was 2.4 times that of the 20-nm-thick BSCF film and 4.7 times that of the bulk BSCF (specific surface area of 0.88 $m^2 g^{-1}$) particle (Fig. 2C). The Tafel slope for the 10-nm-thick BSCF film had the lowest value among all films, which is consistent with this film having the highest intrinsic OER activity (Fig. 2D and fig. S6). The observed optimum intrinsic OER activity trend with increasing thickness differs from the results obtained for BSCF/LSM thin-film electrocatalysts that

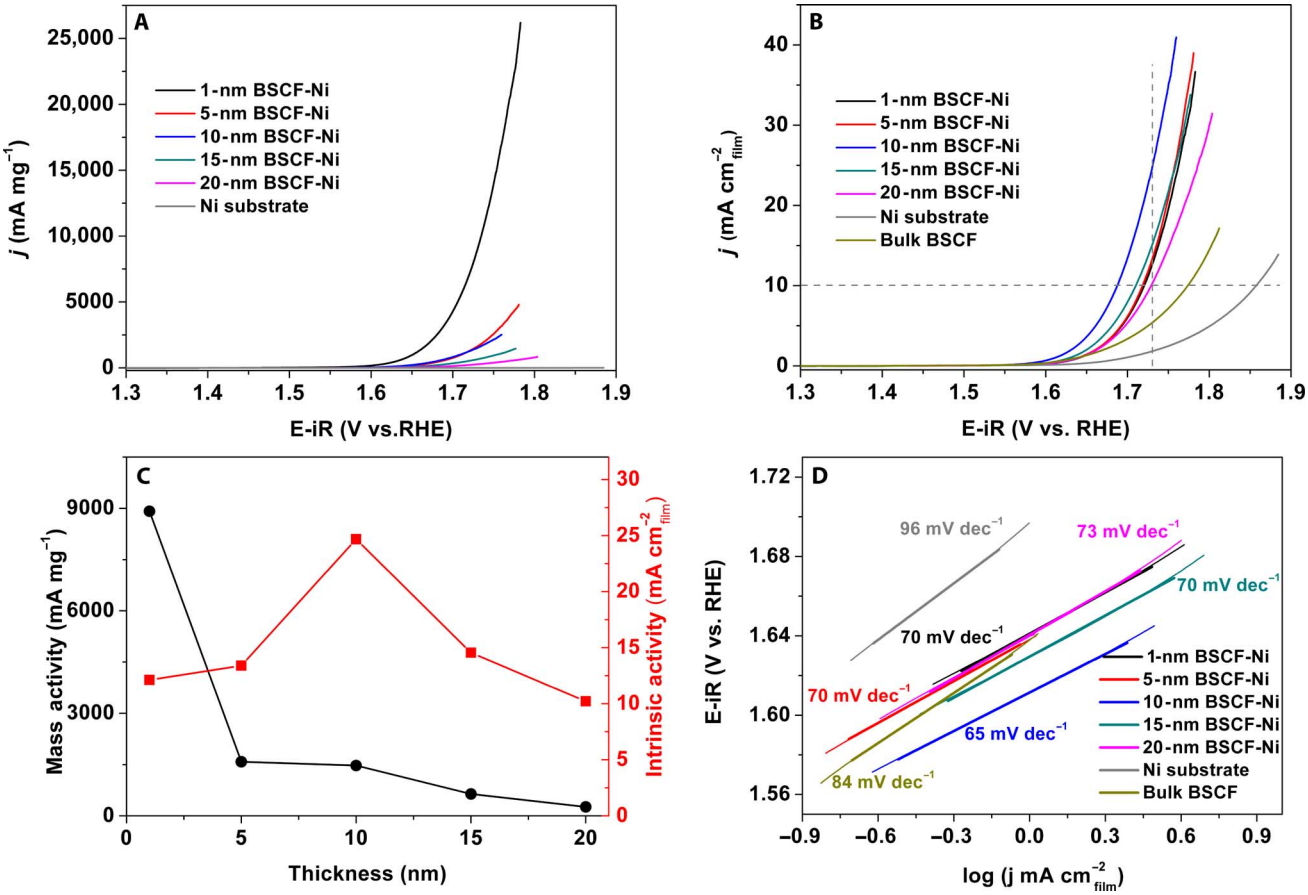

Fig. 2. OER activities of amorphous BSCF nanofilms on Ni foil substrates. (**A**) Mass-normalized activities. (**B**) Intrinsic activities of heterostructures and the bulk BSCF powder. (**C**) Mass and intrinsic activity obtained at η = 0.5 V. (**D**) Tafel plots for the 1-, 5-, 10-, 15-, and 20-nm BSCF–Ni foil heterostructures, Ni substrate, and bulk BSCF powder.

exhibit unchanged intrinsic activities (*15*). The influence of the Ni substrate on the OER performance of the BSCF nanofilms is discussed in the next section.

Correlation between the OER activity and the oxidation states

The OER activity is closely associated with the redox activity of the transition metal ions and therefore their electronic configurations (reflected in oxidation states) (*14*, *25*). XPS was used to probe the chemical states of the transition metal ions in the BSCF nanofilms on Ni foil and the Ni foil substrate (Fig. 1C). The spectra for the Ni substrate contained three different peaks [that is, a peak corresponding to metallic Ni (Ni^0) at 852.1 eV, a peak corresponding to Ni^{2+} at 853.5 eV, and another intense peak corresponding to Ni^{3+} at 855.3 eV] (*26*, *27*). The presence of Ni^{2+} and Ni^{3+} suggests the formation of a nickel oxide layer on top of the Ni foil. The disappearance of the Ni^{3+} peak after further deposition on top of the 1-nm-thick BSCF film (compare 1-nm BSCF-Ni and Ni substrate spectra in Fig. 1C) can only be attributed to the sputtered BSCF layer. This result is consistent with the reduction in the average oxidation state of Ni from 2.68 to 2.30 following the deposition of a 1-nm-thick BSCF film on the Ni substrate (fig. S7). The oxide ions in nickel oxides may diffuse outward onto the sputtered species and eventually oxidize the deposited species. In this case, the deposited species reacts with the oxygen ions originally present in the nickel oxide, reproducing the analogous phenomena previously observed for the pulsed laser deposition of amorphous oxide layer on a $SrTiO_3$ substrate (*28*). Because of the high vacuum and very low Ar pressure applied during the sputtering process, this oxidation effect can only be induced by the oxygen ions from the nickel oxide layer. The Co 2p XPS spectra (Fig. 3A) support this argument and exhibit a subtle shift of both $2p_{3/2}$ and $2p_{1/2}$ peak positions toward higher binding energies as the film thickness decreased. This shift toward higher binding energies, along with the reduction in the satellite peak intensities, indicates the increasing oxidation state of the Co ions to Co^{4+} as the film thickness decreased (*29*, *30*). The Fe 2p XPS spectra also exhibit a similar trend (Fig. 3B).

These observations demonstrate the feasibility of tuning the oxidation states of Co and Fe cations in amorphous BSCF by manipulating the nanofilm thickness. Density functional theory calculations revealed that the binding (adsorption) energy of Co^{3+} to OH^-, which is a typical reaction intermediate in the OER reaction, is relatively low (*25*). However, Co^{4+} forms a strong bond to OH^-, which is reflected by the high Co^{4+}-OH^- binding energy, and hinders OH^- detachment and subsequent oxygen gas release (*14*). This behavior indicates that an optimum oxidation state for Co exists and provides an appropriate binding strength for reaction intermediates to the amorphous BSCF surface (*17*–*20*). Our OER current densities trend exhibit a "volcano" trend with decreasing nanofilm thickness (Fig. 2C), as discussed above. The optimum current density for the 10-nm BSCF–Ni foil heterostructure confirmed the presence of optimized Co and Fe oxidation states at this thickness.

To confirm the critical role of nickel oxides, we removed the nickel oxides on the Ni foil by subjecting the foil to 10 volume % H_2-Ar at 800°C for 1 hour before sputtering (denoted as *x*-nm BSCF–reduced Ni). Following this treatment, the nickel oxides on the surface of the Ni foil were reduced to metallic Ni, leading to thickness-independent Co oxidation state behavior, as revealed by the Co 2p XPS spectra (fig. S8A). The depositions following this treatment result in nearly identical OER activities for different catalyst film thicknesses (fig. S8B). We also deposited 10-nm-thick nickel oxides on top of the Ni foil substrate followed by deposition of a BSCF film (denoted as *x*-nm BSCF–Ni oxide-Ni). Despite the overpotential differences, the area-normalized current densities of these nickel oxide–BSCF films perfectly reproduced the volcano trend we observed for our BSCF-Ni films (fig. S9). The highest activity was exhibited by the 10-nm-thick BSCF film (that is, 10-nm BSCF–Ni oxide–Ni). The intrinsic OER activity of the 10-nm BSCF–Ni oxide–Ni film was even higher than that of the 10-nm BSCF-Ni film. These results unequivocally demonstrate that the deposited species was oxidized by the nickel oxides from the foil (that is, nickel oxides acted as oxygen donors). We did not attempt to deposit more than 10-nm-thick nickel oxide because of its low electrical conductivity, which could have affected the electrochemical performance.

To assess the influence of the substrate on the OER performance tuning, we deposited a BSCF film on an indium tin oxide (ITO) substrate. High mass activities and thickness-dependent, area-normalized OER activities were also observed (figs. S10 and S11 and table S2). In the ITO substrate case, the 2-nm-thick BSCF film exhibited the highest activity, but this activity was lower than the highest activity obtained for 10-nm BSCF-Ni. This result indicates that the nickel oxides are the more efficient substrate agent (relative to Sn and/or In oxide) for optimizing OER catalysis, which was supported by the larger Tafel slopes for ITO and reduced Ni-based BSCF films relative to those for the Ni-based BSCF films (compare fig. S12 with Fig. 2D).

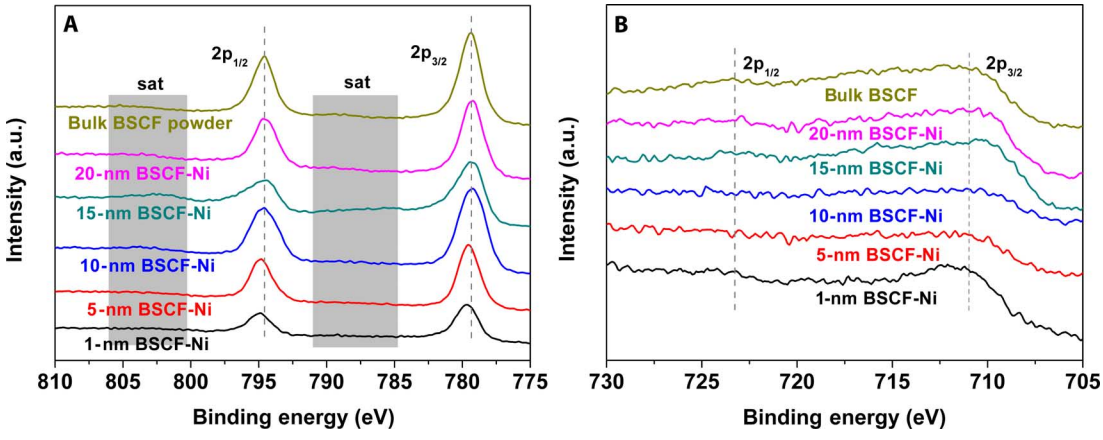

Fig. 3. XPS characterization of amorphous BSCF nanofilms. (**A**) Co 2p and (**B**) Fe 2p XPS for the 1-, 5-, 10-, 15-, and 20-nm BSCF–Ni foil heterostructures as well as the bulk BSCF powder.

OER stability

The stability of the various OER catalysts was assessed by continuous potential cycling between 1.15 and 1.95 V versus RHE in O_2-saturated 0.1 M KOH at room temperature. The comparison of the 1st cycle current profile with the 1000th cycle current profile (fig. S13) revealed an increasing stability as the film thickness increased from 1 to 20 nm. The reduction in the maximum OER current density after 1000 cycles relative to its original maximum current density was 24.8, 9.6, 6.1, and 0.6% for 1, 5, 10, and 15 nm, respectively. Surprisingly, the maximum OER current density increased by 24.7% after 1000 cycles for the 20-nm BSCF film.

For practical applications, a 3D, porous Ni foam substrate is more attractive than Ni foil due to its much higher surface area. We deposited amorphous BSCF onto a Ni foam substrate (denoted as 38.7 μg cm^{-2} BSCF–Ni foam) using the identical deposition parameters relative to the 20-nm-thick film deposition on Ni foil. The as-prepared 38.7 μg cm^{-2} BSCF–Ni foam heterostructured electrode exhibited improved original OER activity compared to that of the 20-nm BSCF–Ni foil heterostructure electrode (compare Fig. 4A with fig. S13E). Because of the larger surface area of the Ni foam compared to that of Ni foil and the same BSCF loading relative to the 20-nm BSCF-Ni case, the BSCF thin film on Ni foam should be thinner than that of the BSCF film on 20-nm BSCF-Ni. The mass activity of the 38.7 μg cm^{-2} BSCF–Ni foam was close to that of 15-nm BSCF-Ni, indicating a similar thickness. The 38.7 μg cm^{-2} BSCF–Ni foam electrode exhibited excellent durability. After 5000 continuous cycles, the OER activity improvement that was previously observed on its Ni foil heterostructured analog was reproduced (compare Fig. 4A with fig. S13E). Prolonging the durability test to 10,000 cycles led to only a slight reduction in the OER activity, and 94% of the original current density was retained. This OER activation process was only observed for the 20-nm-thick BSCF film–based heterostructures. The origin of this activation process in the 20-nm-thick amorphous BSCF layer is not completely clear but may be related to the formation of a sacrificial protective layer, as recently proposed by Zhu *et al.* (*31*). The OER activities of the Ni foil and Ni foam substrates deteriorated after 1000 cycles (fig. S14), ruling out contribution from the Ni substrate to the activation process.

Water splitting

The practical application of the 38.7 μg cm^{-2} BSCF–Ni foam heterostructure anode for water splitting was tested by combining it with the 38.7 μg cm^{-2} Pt–Ni foam cathode to form a two-electrode electrolyzer

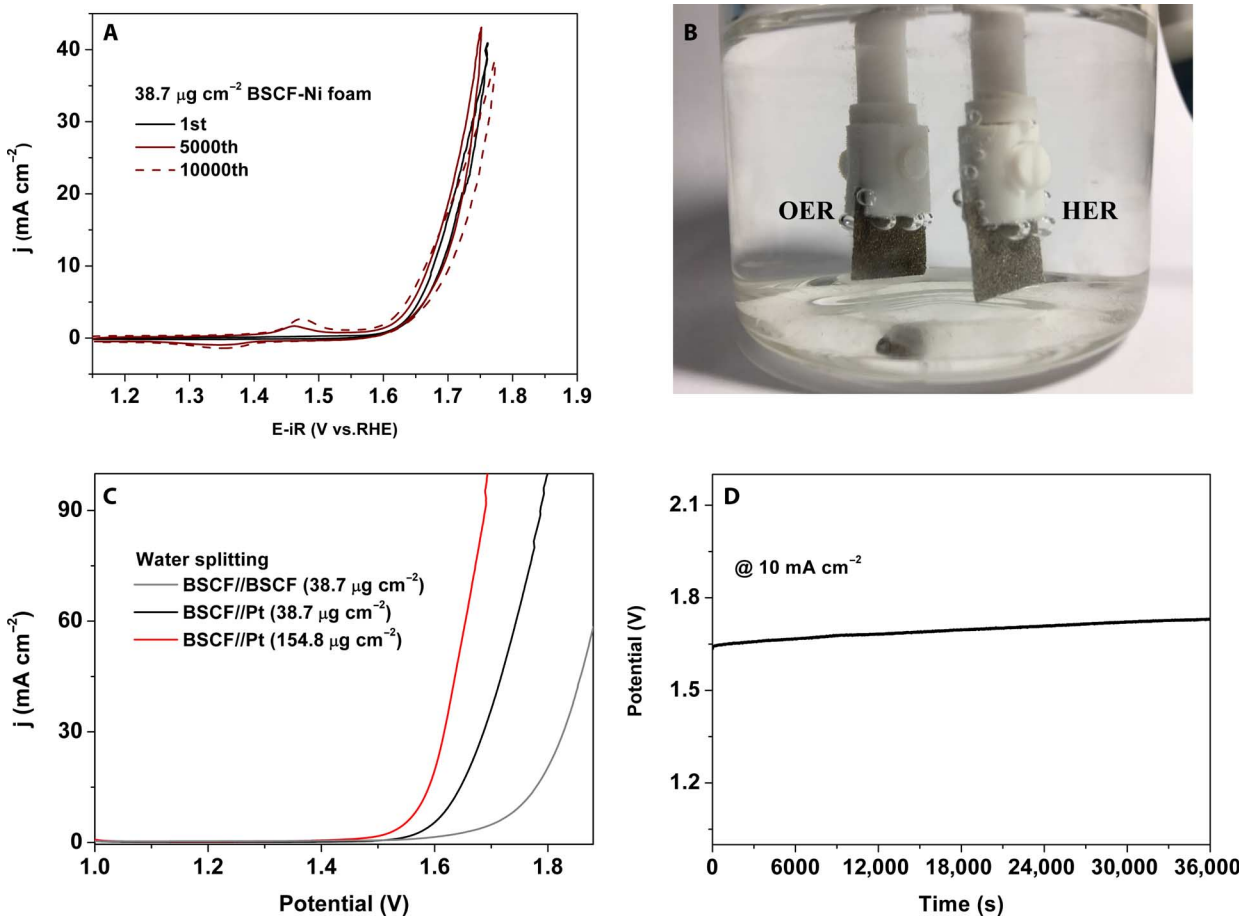

Fig. 4. Electrochemical behaviors of amorphous BSCF nanofilms on Ni foam substrates. (**A**) Current-potential profile at the 1st, 5000th, and 10,000th cycles for the 38.7 μg cm^{-2} BSCF–Ni foam heterostructure electrode in a 0.1 M KOH solution. (**B**) Two-electrode electrolyzer setup consisting of 38.7 μg cm^{-2} BSCF–Ni foam anode and 38.7 μg cm^{-2} Pt–Ni foam cathode in a 1.0 M KOH solution. (**C**) Typical current-potential profiles from the two-electrode electrolyzer during water splitting. (**D**) Time-dependent potential response during 10-hour chronoamperometric water-splitting reaction using the two-electrode electrolyzer (38.7 μg cm^{-2} BSCF–Ni foam anode and 38.7 μg cm^{-2} Pt–Ni foam cathode) at a constant current density of 10 mA cm^{-2}.

in a 1.0 M KOH solution (the OER activity of BSCF–Ni foam in a 1.0 M KOH solution is shown in fig. S15). Figure 4B shows the electrolyzer setup, in which the 38.7 μg cm^{-2} BSCF–Ni foam functioned as the anode for the OER and the 38.7 μg cm^{-2} Pt–Ni foam cathode functioned as the cathode for the HER. For the 38.7 μg cm^{-2} Pt–Ni foam cathode, the Pt deposition on Ni foam was performed by magnetron sputtering. Water splitting has an onset potential of approximately 1.50 V (Fig. 4C). At an applied current density of 10 mA cm^{-2}, water splitting occurred at a potential difference of 1.62 V between the anode and the cathode. The water-splitting reaction can be powered by a single-cell AA battery with a nominal voltage of ≈1.5 V at room temperature (fig. S16 and movie S1). Moreover, the water-splitting performance can be further improved by simply increasing the mass loading to 154.8 μg cm^{-2}. The onset potential was shifted to 1.44 V, and a potential difference of 1.57 V was required to achieve a current density of 10 mA cm^{-2}. The water-splitting performance of our electrolyzer was comparable to that of other water-splitting processes carried out using state-of-the-art catalysts (table S3). However, our electrolyzer was superior in terms of its substantially lower catalyst loading. The chronoamperometric test result for a 10-hour water-splitting reaction only exhibited a moderate increase in potential (that is, by approximately 95 mV) relative to its initial potential (Fig. 4D). The water-splitting performance of 38.7 μg cm^{-2} BSCF–Ni foam as both anode and cathode is shown in Fig. 4C. The lower water-splitting performance is attributed to the lower HER activity for BSCF relative to Pt (*29*). Future works should be focused on developing efficient and stable non–precious metal materials as bifunctional catalysts for water splitting.

DISCUSSION

A facile method has been developed to optimize the OER activities of the amorphous BSCF-Ni heterostructure. All the BSCF nanofilms exhibited excellent mass activities that are superior to the benchmarked IrO_2 catalyst. Moreover, the 10-nm BSCF-Ni catalyst was the best OER catalyst due to the optimized oxidation state of the BSCF nanofilms. The durability appeared to be enhanced as the nanofilm thickness increased. We confirmed the critical role of the nickel oxides on the Ni substrate for tuning the oxidation state of the transition metal cations in the BSCF film. The nickel oxides served as a more efficient substrate agent to maximize the OER activity relative to ITO and metallic nickel. The 20-nm BSCF–Ni foam heterostructure demonstrated excellent durability over 10,000 continuous OER cycles. In addition, we demonstrated the outstanding performance of the 38.7 μg cm^{-2} BSCF–Ni foam heterostructure as an anode component in water splitting using an ultralow mass loading. Our work provides a facile and efficient strategy for obtaining optimum OER activity. This tuning strategy allows for the possible engineering of high electrocatalysis performance using a very low catalyst loading.

MATERIALS AND METHODS

Synthesis of BSCF disc target

The BSCF powder was prepared using a combined EDTA-citrate complexing sol-gel process. Briefly, stoichiometric amounts of $Ba(NO_3)_2$, $Sr(NO_3)_2$, $Co(NO_3)_2{\cdot}6H_2O$, and $Fe(NO_3)_3{\cdot}9H_2O$ (all analytical grade, Sinopharm Chemical Reagent Co. Ltd.) were dissolved in deionized water followed by the addition of a mixture of EDTA ($C_{10}H_{16}N_2O_8$, Sinopharm Chemical Reagent Co. Ltd.) and citric acid ($C_6H_8O_7$, Sinopharm Chemical Reagent Co. Ltd.) as complexing agents at a total metal ion/EDTA/citric acid molar ratio of 1:1:2. To ensure complete complexation, an aqueous ammonium hydroxide solution ($NH_3{\cdot}H_2O$, 28%, Sinopharm Chemical Reagent Co. Ltd.) was added to adjust the solution pH to ~6. The solution was continuously stirred and evaporated at 90°C to yield a clear transparent gel. Then, the gel was heated in an oven at 250°C for 5 hours to form the solid precursor. Calcination was performed using a muffle furnace in air atmosphere at 1000°C for 10 hours to afford the BSCF crystalline powder. Then, the calcined BSCF powder was ground into a fine powder using a mortar and pestle. A dense BSCF disc target was prepared by pressing in a die pellet press set followed by sintering at 1000°C for 10 hours.

Thin-film electrode preparation

The Ni foil (99.99% purity) and Ni foam (99.99% purity) were washed with deionized water and ethanol several times. The amorphous BSCF thin films were deposited onto the substrates using rf magnetron sputtering at an ac power of 40 W in a vacuum chamber with a base pressure of 10^{-3} Pa in an argon (Ar) atmosphere at room temperature. A series of heterostructures with varying BSCF film thicknesses were obtained by increasing the deposition time. The BSCF thin films were deposited on the conductive side of the ITO substrate and two sides of the other substrates. To remove the surface Ni oxide, the Ni foil was reduced in 10% H_2-Ar at 800°C for 1 hour. The 10-nm Ni oxide thin films were deposited onto Ni foils by dc magnetron sputtering at a dc power of 30 W with a metallic Ni target in a 20% O_2:80% Ar atmosphere. The other conditions were the same as those for sputtering amorphous BSCF.

Characterizations

The powder XRD patterns were collected on a Rigaku SmartLab (3 kW) with filtered Cu-Kα radiation (λ = 1.5418 Å). The diffraction patterns were collected by step scanning in a 2θ range of 10° to 90° with an interval of 0.02°. The morphology and elemental distribution were determined using a field-emission SEM equipped with an energy-dispersive spectrometer (FE-SEM-EDS, Hitachi S-4800). The target thickness data were obtained from the film thickness detector system that was installed within the magnetron sputtering and worked by the principle of quartz crystal oscillation. The real film thickness was calibrated on the basis of SEM images. XPS was performed on a PHI 5000 VersaProbe spectrometer equipped with an Al-Kα x-ray source. The XPS analyses were conducted on thin-film samples immediately after the deposition to avoid any change in the oxide film surface during prolonged exposure to the ambient atmosphere. Raman spectroscopy was performed on an HR800 UV Raman microspectrometer (JOBIN YVON). The sample was irradiated by a Melles Griot He/Ne laser at 633 nm. The surface morphological structure of the thin-film samples was further probed by AFM using an AutoProbe CP-Research instrument (AFM) in tapping mode under ambient conditions (that is, air atmosphere and room temperature). The surface areas of thin films were obtained from the AFM data analyzed by NanoScope Analysis. The surface areas of powders were determined by nitrogen adsorption-desorption tests (BELSORP II) using the Brunauer-Emmett-Teller method.

The microgravimetric measurements were performed using a 9-MHz quartz crystal microbalance (QCM) (Princeton Applied Research QCM922). The mass of the film was calculated on the basis of the change in the resonance frequency using the Sauerbrey equation

$$-\Delta F = \frac{2F_0^2}{A\sqrt{\rho_q \mu_q}} \times \Delta m \quad (1)$$

where ΔF is the frequency reduction of the QCM, F_0 is the parent frequency of QCM (9 MHz), A is the area of the gold electrode (0.2 cm^2), ρ_q is the density of quartz (2.65 g cm^{-3}), and μ_q is the shear modulus of quartz (2.95×10^{11} dyne cm^{-2}).

Electrochemical tests

The electrochemical tests were performed at room temperature in a standard three-electrode configuration electrochemical cell that consisted of a thin catalyst film–deposited working electrode, a platinum wire counter electrode, and an Ag/AgCl (3.5 M KCl) reference electrode connected to a CHI 760 E workstation. All potentials were corrected for electrolyte resistance from the high-frequency intercept of the real impedance (~4.5 ohms for 0.1 M KOH and ~2.2 ohms for 1.0 M KOH) and calibrated to the RHE scale [0.950 V (0.1 M KOH) and 1.002 V (1 M KOH) versus RHE is equal to 0 V versus Ag/AgCl (3.5 M KCl)]. Before starting each measurement, 0.1 M KOH electrolyte was bubbled with O_2 for at least 30 min. The cyclic voltammetry (CV) profiles were recorded at a scan rate of 10 mV s^{-1} from 1.15 to 1.95 V versus RHE. Linear sweep voltammetry was performed at a scan rate of 5 mV s^{-1} from 1.0 to 2.0 V (based on the potential difference between the two electrodes) for the water-splitting test. The high mass loading samples were derived from pressing four Ni foams together. For the stability test, the CV measurements were obtained at a scan rate of 100 mV s^{-1}. The long-term durability test for water splitting was performed using chronopotentiometric measurements at a current density of 10 mA cm^{-2} for 10 hours. The traditional rotating disk electrode test was performed according to previously reported protocols (*31*, *32*).

SUPPLEMENTARY MATERIALS

Supplementary material for this article is available at http://advances.sciencemag.org/cgi/content/full/3/6/e1603206/DC1

fig. S1. Powder XRD patterns of the crystalline BSCF perovskite target.
fig. S2. Surface morphology obtained by AFM on the top of Ni foil.
fig. S3. SEM image of the amorphous BSCF nanofilm and the respective energy-dispersive x-ray spectrum.
fig. S4. SEM images of the film/substrate interface on the top of silicon wafer.
fig. S5. Basic characterizations and OER activity of bulk IrO_2.
fig. S6. Tafel slopes for mass activities of amorphous BSCF on Ni foil substrates.
fig. S7. Ni 2p XPS.
fig. S8. XPS and OER results of reduced Ni-based nanofilms.
fig. S9. OER activities of Ni oxide–based nanofilms.
fig. S10. XPS results of ITO-based nanofilms.
fig. S11. Mass activities for BSCF-ITO heterostructures.
fig. S12. Tafel plots.
fig. S13. Stability tests of nanofilms.
fig. S14. Stability tests of Ni foil and Ni foam.
fig. S15. OER activity for the 38.7 and 154.8 μg cm^{-2} BSCF–Ni foam heterostructure electrodes in a 1.0 M KOH solution.
fig. S16. Photograph of a water-splitting device.
table S1. Comparison of the mass activities of the thin-film heterostructures to other recently reported catalysts for the OER in an alkaline solution.
table S2. Comparison of the overpotentials to obtain 10 mA cm^{-2}_{film} for the ITO-based heterostructures and the Ni foil–based heterostructures.
table S3. Comparison of the performance of the water-splitting catalysts in a 1.0 M KOH solution.
movie S1. Video of a water-splitting device.
References (*33*–*47*)

REFERENCES AND NOTES

1. D. Chen, C. Chen, Z. M. Baiyee, Z. Shao, F. Ciucci, Nonstoichiometric oxides as low-cost and highly-efficient oxygen reduction/evolution catalysts for low-temperature electrochemical devices. *Chem. Rev.* **115**, 9869–9921 (2015).
2. Z. Shao, W. Zhou, Z. Zhu, Advanced synthesis of materials for intermediate-temperature solid oxide fuel cells. *Prog. Mater. Sci.* **57**, 804–874 (2012).
3. W. Zhou, Y. Jiao, S.-D. Li, Z. Shao, Anodes for carbon-fueled solid oxide fuel cells. *ChemElectroChem* **3**, 193–203 (2016).
4. X. Cui, P. Ren, D. Deng, J. Deng, X. Bao, Single layer graphene encapsulating non-precious metals as high-performance electrocatalysts for water oxidation. *Energy Environ. Sci.* **9**, 123–129 (2016).
5. N. Danilovic, R. Subbaraman, K. C. Chang, S. H. Chang, Y. Kang, J. Snyder, A. P. Paulikas, D. Strmcnik, Y. T. Kim, D. Myers, V. R. Stamenkovic, N. M. Markovic, Using surface segregation to design stable Ru-Ir oxides for the oxygen evolution reaction in acidic environments. *Angew. Chem. Int. Ed.* **126**, 14240–14245 (2014).
6. S. H. Chang, N. Danilovic, K.-C. Chang, R. Subbaraman, A. P. Paulikas, D. D. Fong, M. J. Highland, P. M. Baldo, V. R. Stamenkovic, J. W. Freeland, J. A. Eastman, N. M. Markovic, Functional links between stability and reactivity of strontium ruthenate single crystals during oxygen evolution. *Nat. Commun.* **5**, 4191 (2014).
7. J. Rossmeisl, A. Logadottir, J. K. Nørskov, Electrolysis of water on (oxidized) metal surface. *Chem. Phys.* **319**, 178–184 (2005).
8. K. J. May, C. E. Carlton, K. A. Stoerzinger, M. Risch, J. Suntivich, Y.-L. Lee, A. Grimaud, Y. Shao-Horn, Influence of oxygen evolution during water oxidation on the surface of perovskite oxide catalysts. *J. Phys. Chem. Lett.* **3**, 3264–3270 (2012).
9. P. Liao, J. A. Keith, E. A. Carter, Water oxidation on pure and doped hematite (0001) surfaces: Prediction of Co and Ni as effective dopants for electrocatalysis. *J. Am. Chem. Soc.* **134**, 13296–13309 (2012).
10. H. B. Tao, L. Fang, J. Chen, H. B. Yang, J. Gao, J. Miao, S. Chen, B. Liu, Identification of surface reactivity descriptor for transition metal oxides in oxygen evolution reaction. *J. Am. Chem. Soc.* **138**, 9978–9985 (2016).
11. Z. Shao, S. M. Haile, A high-performance cathode for the next generation of solid-oxide fuel cells. *Nature* **431**, 170–173 (2004).
12. Z. Shao, W. Yang, Y. Cong, H. Dong, J. Tong, G. Xiong, Investigation of the permeation behavior and stability of a $Ba_{0.5}Sr_{0.5}Co_{0.8}Fe_{0.2}O_{3-\delta}$ oxygen membrane. *J. Membr. Sci.* **172**, 177–188 (2000).
13. J. Suntivich, K. J. May, H. A. Gasteiger, J. B. Goodenough, Y. Shao-Horn, A perovskite oxide optimized for oxygen evolution catalysis from molecular orbital principles. *Science* **334**, 1383–1385 (2011).
14. C. Zhang, C. P. Berlinguette, S. Trudel, Water oxidation catalysis: An amorphous quaternary Ba-Sr-Co-Fe oxide as a promising electrocatalyst for the oxygen-evolution reaction. *Chem. Commun.* **52**, 1513–1516 (2016).
15. M. Risch, K. A. Stoerzinger, S. Maruyama, W. T. Hong, I. Takeuchi, Y. Shao-Horn, $La_{0.8}Sr_{0.2}MnO_{3-\delta}$ decorated with $Ba_{0.5}Sr_{0.5}Co_{0.8}Fe_{0.2}O_{3-\delta}$: A bifunctional surface for oxygen electrocatalysis with enhanced stability and activity. *J. Am. Chem. Soc.* **136**, 5229–5232 (2014).
16. D. V. Esposito, S. T. Hunt, A. L. Stottlemyer, K. D. Dobson, B. E. McCandless, R. W. Birkmire, J. G. Chen, Low-cost hydrogen-evolution catalysts based on monolayer platinum on tungsten monocarbide substrates. *Angew. Chem. Int. Ed.* **49**, 9859–9862 (2010).
17. J. O. Bockris, T. Otagawa, Mechanism of oxygen evolution on perovskites. *J. Phys. Chem.* **87**, 2960–2971 (1983).
18. S. Trasatti, Electrocatalysis in the anodic evolution of oxygen and chloride. *Electrochim. Acta* **29**, 1503–1512 (1984).
19. J. Rossmeisl, Z.-W. Qu, H. Zhu, G.-J. Kroes, J. K. Nørskov, Electrolysis of water on oxide surfaces. *J. Electroanal. Chem.* **607**, 83–89 (2007).
20. I. C. Man, H.-Y. Su, F. Calle-Vallejo, H. A. Hansen, J. I. Martínex, N. G. Inoglu, J. Kitchin, T. F. Jaramillo, J. K. Nørskov, J. Rossmeisl, Universality in oxygen evolution electrocatalysis on oxide surfaces. *ChemCatChem* **3**, 1159–1165 (2011).
21. S. Gangopadhayay, T. Inerbaev, A. E. Masunov, D. Altilio, N. Orlovskaya, Structural characterization combined with the first principles simulations of barium/strontium cobaltite/ferrite as promising material for solid oxide fuel cells cathodes and high-temperature oxygen permeation membranes. *ACS Appl. Mater. Interfaces* **1**, 1512–1519 (2009).
22. Y. Lee, J. Suntivich, K. J. May, E. E. Perry, Y. Shao-Horn, Synthesis and activities of rutile IrO_2 and RuO_2 nanoparticles for oxygen evolution in acid and alkaline solutions. *J. Phys. Chem. Lett.* **3**, 399–404 (2012).
23. Y. Zhu, W. Zhou, Z.-G. Chen, Y. Chen, C. Su, M. O. Tadé, Z. Shao, $SrNb_{0.1}Co_{0.7}Fe_{0.2}O_{3-\delta}$ perovskite as a next-generation electrocatalyst for oxygen evolution in alkaline solution. *Angew. Chem. Int. Ed.* **54**, 3897–3901 (2015).
24. Y. Matsumoto, E. Sato, Electrocatalytic properties of transition metal oxides for oxygen evolution reaction. *Mater. Chem. Phys.* **14**, 397–426 (1986).
25. B. Zhang, X. Zheng, O. Voznyy, R. Comin, M. Bajdich, M. García-Melchor, L. Han, J. Xu, M. Liu, L. Zheng, F. P. García de Arquer, C. T. Dinh, F. Fan, M. Yuan, E. Yassitepe, N. Chen, T. Regier, P. Liu, Y. Li, P. De Luna, A. Janmohamed, H. L. Xin, H. Yang, A. Vojvodic, E. H. Sargent, Homogeneously dispersed multimetal oxygen-evolving catalysts. *Science* **352**, 333–337 (2016).
26. M. Gong, W. Zhou, M.-C. Tsai, J. Zhou, M. Guan, M.-C. Lin, B. Zhang, Y. Hu, D.-Y. Wang, J. Yang, S. J. Pennycook, B.-J. Hwang, H. Dai, Nanoscale nickel oxide/nickel heterostructures for active hydrogen evolution electrocatalysis. *Nat. Commun.* **5**, 4695 (2014).

27. C. Yuan, J. Li, L. Hou, X. Zhang, L. Shen, X. W. D. Lou, Ultrathin mesoporous $NiCo_2O_4$ nanosheets supported on Ni foam as advanced electrodes for supercapacitors. *Adv. Funct. Mater.* **22**, 4592–4597 (2012).
28. Y. Chen, N. Pryds, J. E. Kleibeuker, G. Koster, J. Sun, E. Stamate, B. Shen, G. Rijnders, S. Linderoth, Metallic and insulating interfaces of amorphous $SrTiO_3$-based oxide heterostructures. *Nano Lett.* **11**, 3774–3778 (2011).
29. X. Xu, Y. Chen, W. Zhou, Z. Zhu, C. Su, M. Liu, Z. Shao, A perovskite electrocatalyst for efficient hydrogen evolution reaction. *Adv. Mater.* **28**, 6442–6448 (2016).
30. Y. Zhu, W. Zhou, Y. Chen, J. Yu, M. Liu, Z. Shao, A High-performance electrocatalyst for oxygen evolution reaction: $LiCo_{0.8}Fe_{0.2}O_2$. *Adv. Mater.* **27**, 7150–7155 (2015).
31. Y. Zhu, W. Zhou, J. Sunarso, Y. Zhong, Z. Shao, Phosphorus-doped perovskite oxide as highly efficient water oxidation electrocatalyst in alkaline solution. *Adv. Funct. Mater.* **26**, 5862–5872 (2016).
32. G. Chen, J. Sunarso, Y. Zhu, J. Yu, Y. Zhong, W. Zhou, Z. Shao, Highly active carbon/α-MnO_2 hybrid oxygen reduction reaction electrocatalysts. *ChemElectroChem* **3**, 1760–1767 (2016).
33. X. Xu, C. Su, W. Zhou, Y. Zhu, Y. Chen, Z. Shao, Co-doping strategy for developing perovskite oxides as highly efficient electrocatalysts for oxygen evolution reaction. *Adv. Sci.* **3**, 1500187 (2016).
34. S. Zhou, X. Miao, X. Zhao, C. Ma, Y. Qiu, Z. Hu, J. Zhao, S. Lei, J. Zeng, Engineering electrocatalytic activity in nanosized perovskite cobaltite through surface spin-state transition. *Nat. Commun.* **7**, 11510 (2016).
35. C.-W. Tung, Y.-Y. Hsu, Y.-P. Shen, Y. Zheng, T.-S. Chan, H.-S. Sheu, Y.-C. Cheng, H. M. Chen, Reversible adapting layer produces robust single-crystal electrocatalyst for oxygen evolution. *Nat. Commun.* **6**, 8106 (2015).
36. L. Trotochaud, J. K. Ranney, K. N. Williams, S. W. Boettcher, Solution-cast metal oxide thin film electrocatalysts for oxygen evolution. *J. Am. Chem. Soc.* **134**, 17253–17261 (2012).
37. F. Liang, Y. Yu, W. Zhou, X. Xu, Z. Zhu, Highly defective CeO_2 as a promoter for efficient and stable water oxidation. *J. Mater. Chem. A* **3**, 634–640 (2015).
38. J. Huang, J. Chen, T. Yao, J. He, S. Jiang, Z. Sun, Q. Liu, W. Cheng, F. Hu, Y. Jiang, Z. Pan, S. Wei, CoOOH nanosheets with high mass activity for water oxidation. *Angew. Chem. Int. Ed.* **127**, 8846–8851 (2015).
39. J. Kim, X. Yin, K.-C. Tsao, S. Fang, H. Yang, $Ca_2Mn_2O_5$ as oxygen-deficient perovskite electrocatalyst for oxygen evolution reaction. *J. Am. Chem. Soc.* **136**, 14646–14649 (2014).
40. N. Jiang, B. You, M. Sheng, Y. Sun, Electrodeposited cobalt-phosphorous-derived films as competent bifunctional catalysts for overall water splitting. *Angew. Chem. Int. Ed.* **54**, 6251–6254 (2015).
41. G.-F. Chen, T. Y. Ma, Z.-Q. Liu, N. Li, Y.-Z. Su, K. Davey, S.-Z. Qiao, Efficient and stable bifunctional electrocatalysts Ni/Ni_xM_y (M= P, S) for overall water splitting. *Adv. Funct. Mater.* **26**, 3314–3323 (2016).
42. Z. Peng, D. Jia, A. M. Al-Enizi, A. A. Elzatahry, G. Zheng, From water oxidation to reduction: Homologous Ni-Co based nanowires as complementary water splitting electrocatalysts. *Adv. Energy Mater.* **5**, 1402031 (2015).
43. C. Tang, N. Cheng, Z. Pu, W. Xing, X. Sun, NiSe nanowire film supported on nickel foam: An efficient and stable 3D bifunctional electrode for full water splitting. *Angew. Chem. Int. Ed.* **54**, 9351–9355 (2015).
44. J. Wang, H.-x. Zhong, Z.-l. Wang, F.-l. Meng, X.-b. Zhang, Integrated three-dimensional carbon paper/carbon tubes/cobalt-sulfide sheets as an efficient electrode for overall water splitting. *ACS Nano* **10**, 2342–2348 (2016).
45. Y. Hou, M. R. Lohe, J. Zhang, S. Liu, X. Zhuang, X. Feng, Vertically oriented cobalt selenide/NiFe layered-double-hydroxide nanosheets supported on exfoliated graphene foil: An efficient 3D electrode for overall water splitting. *Energy Environ. Sci.* **9**, 478–483 (2016).
46. M. Ledendecker, S. K. Calderón, C. Papp, H.-P. Steinrück, M. Antonietti, M. Shalom, The synthesis of nanostructured Ni_5P_4 films and their use as a non-noble bifunctional electrocatalyst for full water splitting. *Angew. Chem. Int. Ed.* **127**, 12538–12542 (2015).
47. Y. Zhu, W. Zhou, Y. Zhong, Y. Bu, X. Chen, Q. Zhong, M. Liu, Z. Shao, A perovskite nanorod as bifunctional electrocatalyst for overall water splitting. *Adv. Energy Mater.* **7**, 1602122 (2017).

Acknowledgments

Funding: This work was financially supported by the National Nature Science Foundation of China under contract no. 21576135, the Priority Academic Program Development of Jiangsu Higher Education Institutions, the Changjiang Scholars Program and the Program for Jiangsu Specially-Appointed Professors, and the Youth Fund in Jiangsu Province under contract no. BK20150945. **Author contributions:** G.C. and W. Zhou conceived and designed the project. G.C. and D.G. carried out the target syntheses and conducted the sputtering experiments. G.C. and Y.Z. conducted the characterization. G.C. developed the electrochemical measurements. X.H. and W. Zhang provided consultation. G.C., W. Zhou, J.S., and Z.S. co-wrote the paper. All authors discussed the results and commented on the manuscript. **Competing interests:** The authors declare that they have no competing interests. **Data and materials availability:** All data needed to evaluate the conclusions in the paper are present in the paper and/or the Supplementary Materials. Additional data related to this paper may be requested from the authors.

Submitted 16 December 2016
Accepted 1 May 2017
Published 21 June 2017
10.1126/sciadv.1603206

Citation: G. Chen, W. Zhou, D. Guan, J. Sunarso, Y. Zhu, X. Hu, W. Zhang, Z. Shao, Two orders of magnitude enhancement in oxygen evolution reactivity on amorphous $Ba_{0.5}Sr_{0.5}Co_{0.8}Fe_{0.2}O_{3-\delta}$ nanofilms with tunable oxidation state. *Sci. Adv.* **3**, e1603206 (2017).

Science Advances

Two orders of magnitude enhancement in oxygen evolution reactivity on amorphous $Ba_{0.5}Sr_{0.5}Co_{0.8}Fe_{0.2}O_{3-\delta}$ nanofilms with tunable oxidation state

Gao Chen, Wei Zhou, Daqin Guan, Jaka Sunarso, Yanping Zhu, Xuefeng Hu, Wei Zhang and Zongping Shao

Sci Adv **3** (6), e1603206.
DOI: 10.1126/sciadv.1603206